Active Power Decoupling Method Using a Center-Tap DAB Matrix Converter Without Additional Switches

Kousei Irimura
Department of Science of Technology Innovation
Nagaoka University of Technology
Nagaoka, Japan
s223133@stn.nagaokaut.ac.jp

Masamichi Yamaguchi
Department of Science of Technology Innovation
Nagaoka University of Technology
Nagaoka, Japan
m_yamaguchi@stn.nagaokaut.ac.jp

Hiroki Watanabe
Department of Electrical, Electronics and Information Engineering
Nagaoka University of Technology
Nagaoka, Japan
hwatanabe@vos.nagaokaut.ac.jp

Jun-ichi Itoh
Department of Science of Technology Innovation
Nagaoka University of Technology
Nagaoka, Japan
itoh@vos.nagaokaut.ac.jp

Abstract—**This paper proposes an active power decoupling (APD) method for a dual-active-bridge (DAB) matrix converter. The proposed method compensates for the second-harmonic power ripple that appears during single-phase operation while sharing circuit components with the existing three-phase configuration, thereby reducing the overall component count. The proposed APD approach does not require any additional switching devices because the buffer current is controlled through a center-tap circuit on the secondary side of the transformer. Experimental results demonstrate that the proposed method reduces the 100 Hz ripple component in the output current by 82% and achieves a power factor of 0.99 under a 500 W power transfer condition.**

Keywords—DAB converter，Matrix converter, Active power decoupling，three/single-phase switchable

I. INTRODUCTION

In recent years, the adoption of electric vehicles (EVs) in Europe has rapidly increased because of stricter regulations on carbon emissions [1]. The residential distribution system in Europe allows users to choose between a three-phase and a single-phase grid connection. Therefore, the on-board charger (OBC) of an EV must be compatible with both types of grid connections. In many countries, three-phase grids are commonly used at public fast-charging facilities, whereas single-phase grids are prevalent in residential areas. Supporting both grid types reduces constraints on charging infrastructure and facilitates broader EV adoption [2]. Since EVs are typically connected to the grid for extended periods in residential settings, methods for utilizing the EV battery to support the grid have also been proposed [3], [4]. Consequently, OBCs must also provide bidirectional power-transfer capability.

In particular, a double-frequency power ripple appears when an OBC is connected to a single-phase grid, and this ripple must be compensated. A simple approach is to passively absorb this ripple using a large capacitor. This approach typically requires an electrolytic capacitor, which has a limited lifetime. As a result, the reliability of the OBC significantly reduced [5].

An alternative is active power decoupling (APD), which actively controls the buffer-capacitor current using semiconductor switches [6]. APD increases the effective capacitance by intentionally allowing a voltage ripple on the capacitor voltage. Consequently, the power ripple can be compensated with a small capacitor, eliminating the need for a large electrolytic capacitor. Several methods that incorporate APD into converters compatible with both grid types have been proposed [7], [8].

Reference [7] has proposed an OBC that uses three interleaved totem-pole isolated AC–DC converter modules connected in parallel. When connected to a three-phase grid, each module generates a sinusoidal output that is phase-shifted by 120 degrees. This operation distributes the load and enables high-power charging. In a single-phase configuration, two modules are used for AC–DC conversion, whereas the remaining module operates as a buffer circuit to compensate for the power ripple. All switches achieve zero-voltage switching (ZVS), and APD is realized simply by adding a buffer capacitor. However, this circuit requires numerous inductors and transformers, and the additional magnetic components increase the component count and making the circuit more complex and bulky.

Reference [8] proposes a resonant AC–DC converter that employs a three-phase-to-single-phase matrix converter. This approach reduces the number of passive components, such as boost inductors, by utilizing the matrix converter. When the system is connected to a single-phase grid, APD is achieved by controlling the current through the input-filter capacitor using switches that are not connected to the grid. This implementation does not require dedicated switches for power-ripple compensation. However, the power factor deteriorates significantly because the input filter capacitor also serves as the buffer capacitor. The novelty of this study lies in demonstrating that a center-tap architecture can be utilized to realize active power decoupling in a DAB matrix converter, achieving effective ripple compensation without increasing the number of switching devices.

This paper proposes a dual-active-bridge-type matrix converter that compensates single-phase power ripple without requiring additional switches and at the same time achieves a high power factor. Experimental verification using a small-scale prototype confirms the effectiveness of the proposed method.

II. PROPOSED A DAB MATRIX CONVERTER WITH A CENTER-TAPPED TRANSFORMER

A. Circuit Configuration

Figure 1 shows the proposed dual-active-bridge-type

XXX-X-XXXX-XXXX-X/XX/$XX.00 ©20XX IEEE

matrix converter that supports both three-phase and single-phase inputs. The secondary side of the high-frequency transformer includes a center tap. A buffer circuit, which is composed of a buffer capacitor and an inductor, is connected to the tap to compensate for the single-phase power ripple. The secondary-side inverter controls the current between the DC voltage source and the buffer circuit, and the power ripple is compensated through this current control. Power ripple compensation is achieved with a high power factor because the buffer circuit is isolated from the primary side. Furthermore, additional switches are not required for controlling the buffer circuit current. The matrix converter also reduces the number of large passive components. As a result, the component count is lower than that of conventional interleaved totem-pole approaches.

B. Control Method with a Three-phase Grid

When the proposed circuit is connected to a three-phase grid, the grid current is controlled using space vector modulation (SVM). However, the transformer current is not constant due to the dual-active-bridge structure of the proposed converter. Therefore, the duty ratios calculated by SVM cannot be directly applied. Thus, duty ratios must be corrected to generate the current vectors I_1 and I_2 defined by SVM [9].

Figure 2 shows the output voltages of the matrix converter and the inverter in a three-phase grid, along with the corresponding transformer current waveforms. The output intervals within one switching period and their respective durations and duty ratios are defined as T_a, T_1, T_2, T_b, T_0, and D_a, D_1, D_2, D_b, D_0, respectively. The instantaneous transformer currents during each interval are defined as i_1, i_2, and i_3. Assuming the initial current i_0 is zero, the relationship between the transformer currents and the current vectors derived from SVM is expressed by

$$I_1 = \frac{i_1}{2} D_a + \frac{i_1 + i_2}{2} D_1 \quad \text{...}(1),$$

$$I_2 = \frac{i_2 + i_3}{2} D_2 \quad \text{...}(2).$$

The duty ratios are obtained by substituting the leakage inductance and the output voltages into (1) and (2) as

$$D_1 = \sqrt{\frac{4 I_1 L f_{sw}}{v_{\max}(a+1)^2 - NV_{dc}}} \quad \because a = \frac{D_a}{D_1} \quad \text{............................}(3),$$

$$D_2 = \left(-b \pm \sqrt{b^2 - 4c}\right) \frac{D_1}{2}$$
$$\because b = \frac{v_{\max}(a+1) - NV_{dc}}{v_{mid} - NV_{dc}}, \quad c = \frac{I_2}{I_1} \frac{v_{\max}(a+1)^2 - NV_{dc}}{v_{mid} - NV_{dc}} \quad \text{..........}(4),$$

$$D_b = \frac{\left(v_{\max}(a+1) - NV_{dc}\right) D_1 + \left(v_{mid} - NV_{dc}\right) D_2}{NV_{dc}} \quad \text{......................}(5),$$

where $v_{\max}$ denotes the maximum line-to-line voltage, and v_{mid} denotes the intermediate line-to-line voltage. The coefficient a is a parameter determined by the output power and the DC voltage.

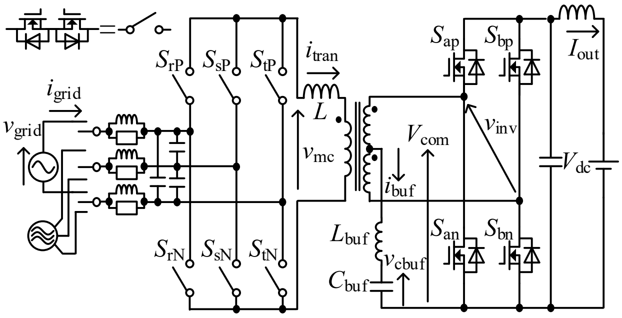

Fig. 1. Proposed isolated DAB-type AC-DC converter.

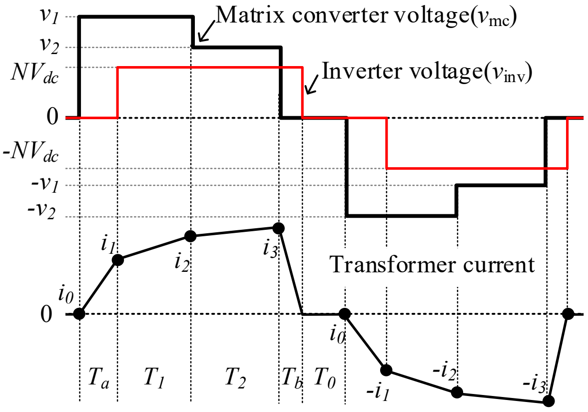

Fig. 2. High-frequency voltage and current waveforms.

III. PROPOSED METHOD WITH SINGLE-PHASE GRID

A. Matrix Converter Control Based on Virtual Indirect Conversion

Figure 3 shows the block diagram of the proposed control method. The proposed method is based on a virtual AC–DC–AC conversion with a carrier comparison, which is one of the control techniques used for matrix converters [10]. The input and output waveform controls interfere with each other because a matrix converter does not have an energy buffer. To address this issue, the rectifier control is applied to a virtual current-source inverter, while the inverter control is applied to a virtual voltage-source inverter. The virtual PWM rectifier operates in synchronous rectification mode, and the power factor is controlled accordingly. Bidirectional power transfer is achieved by operating the virtual inverter as a two-level converter with single-sided PWM modulation, thereby realizing dual-active-bridge operation through this modulation strategy.

B. Zero-voltage Period

The voltage amplitude difference between the primary and secondary sides of the transformer increases near the zero crossing of the grid voltage. As a result, the peak value of the transformer current becomes larger, and inrush current appears at the zero crossing of the grid current. The zero-voltage period of the secondary-side inverter is determined through simulation so that this interval becomes longer near the zero crossing, where the voltage difference between the grid voltage peak and the DC voltage is small. The zero-voltage period is defined by

$$\varepsilon = T_{\text{sw}} \left| \frac{NV_{\text{dc}} - \sqrt{2} V_{\text{g}} \sin(\omega_0 t)}{\sqrt{2} V_{\text{g}}} \right| \quad \text{...................................}(6),$$

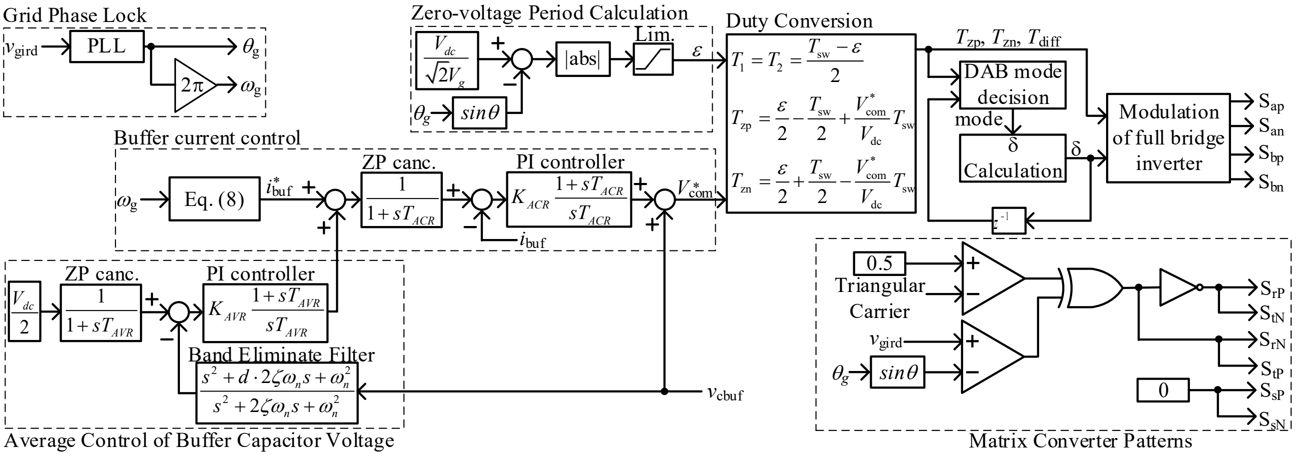

Fig. 3. A control block diagram of the proposed converter.

where ε denotes the zero-voltage period, N is the transformer turns ratio, $T_{\rm sw}$ is the control period, and $V_{\rm g}$ is the RMS value of the grid voltage.

C. Power Ripple Compensation Quantity

The buffer capacitor voltage is intentionally allowed to ripple by controlling the buffer current $i_{\rm buf}$, which flows into the buffer circuit and is connected to the center-tap on the secondary side in the proposed circuit. This operation compensates for the power ripple that arises when the converter is connected to a single-phase grid under unity power factor conditions. The instantaneous input power is expressed by

$$\begin{aligned} p_{\rm g} &= 2V_{\rm g}I_{\rm g}\sin^2(\omega_0 t) \\ &= V_{\rm g}I_{\rm g} - V_{\rm g}I_{\rm g}\cos(2\omega_0 t) = P_{\rm ave}\{1-\cos(2\omega_0 t)\} \end{aligned} \quad ....(7),$$

where $I_{\rm g}$ is the RMS value of the grid current, $P_{\rm ave}$ is the average output power, and ω_0 is the grid angular frequency. The second term in (7) represents the power ripple component that must be compensated. The reference buffer current $i_{\rm buf}^*$ is derived to cancel this component. The buffer capacitor voltage is determined based on the energy that the capacitor must store. The buffer current command $i_{\rm buf}^*$ is calculated from the voltage–current relationship, as shown in

$$i_{\rm buf}^* = \frac{P_{\rm ave}\cos(2\omega_0 t)}{\sqrt{\left(\frac{V_{\rm dc}}{2}\right)^2 + \frac{P_{\rm ave}}{\omega_0 C_{\rm buf}}\sin(2\omega_0 t)}} \quad ....(8).$$

D. Power Ripple Compensation Method With a Center-Tap

Figures 4(a) and 4(b) show the switching patterns in which a voltage is applied to the secondary winding of the transformer. These patterns are defined as differential-pattern modes that contribute to power transfer. The neutral potential is equal to the secondary neutral point voltage $V_{\rm dc}/2$ during the differential-patterns mode output. Therefore, the buffer current remains unchanged.

In contrast, Figures 4(c) and 4(d) show switching patterns where the voltage applied to the secondary winding becomes zero. These patterns are defined as common-mode patterns, which do not contribute to power transfer. Since no voltage is applied to the secondary winding during the common-mode patterns, no current flows to the DC side. The common-mode patterns include two operating modes related to the N arm of the secondary-side inverter. In the charging mode, the DC voltage $V_{\rm dc}$ is applied to the center-tap when the upper switch is on. In the discharging mode, a zero-voltage is applied when the lower switch is on. The center-tap voltage $V_{\rm com}$ is controlled by switching between the charging and discharging modes. The buffer current is regulated through this operation, thereby compensating for the power ripple.

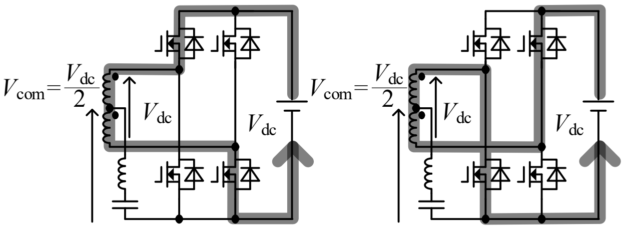

(a) Plus differential (b) Minus differential

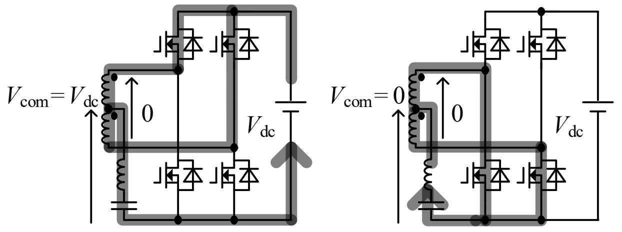

(c)Upper common (d) Lower common

Fig. 4. Configuration of the pattern for the DC side.

Figure 5 shows the operating waveforms of the transformer voltages on both the primary and secondary sides, as well as the center-tap voltage $V_{\rm com}$ during power transfer. The secondary-side inverter alternately outputs the charging mode $T_{\rm zp}$ and the discharging mode $T_{\rm zn}$ of the common-mode pattern during the differential pattern intervals T_1 and T_2.

The center-tap voltage is expressed as the periodic average of the output voltages resulting from both the common-mode and differential patterns. The relationship among the center-tap voltage, the differential pattern intervals, and the charging and discharging intervals of the common-mode patterns is given in

$$V_{\rm com} = \left(\frac{V_{\rm dc}}{2}T_1 + \frac{V_{\rm dc}}{2}T_2 + V_{\rm dc}T_{\rm zp} + 0\cdot T_{\rm zn}\right)\frac{1}{T_{\rm sw}} \quad ....(9).$$

The output duration of the common-mode pattern must lie within the zero-voltage period defined by (6). Additionally, each output interval must match the control period, and the voltage-time product across the transformer must be zero. Subject to these constraints, the output durations of each mode that generate the center-tap voltage, which is used as the control variable for the buffer current, are expressed by

$$T_1 = T_2 = \frac{T_{sw} - \varepsilon}{2} \quad \text{..}(10),$$

$$T_{zp} = \frac{\varepsilon}{2} - \frac{T_{sw}}{2} + \frac{V_{com}^*}{V_{dc}} T_{sw} \quad \text{...}(11),$$

$$T_{zn} = \frac{\varepsilon}{2} + \frac{T_{sw}}{2} - \frac{V_{com}^*}{V_{dc}} T_{sw} \quad \text{...}(12).$$

E. Transmission Power Control via Primary–Secondary Phase Shift

Figure 6 shows the transformer voltage and current waveforms of the matrix converter and the secondary-side inverter during power transfer. The output durations of the charging and discharging modes are equal, and the phase difference between the primary and secondary sides is less than half of the zero-voltage period in the illustrated operation. The output voltage of the matrix converter can be considered constant over one control period, as the grid frequency is sufficiently lower than the switching frequency.

The real power of the dual-active-bridge converter is obtained by averaging the time integrals of the transformer voltage and current over the control period for each operating mode. The instantaneous transformer current in each mode is expressed by using the initial current i_0 as

$$i_{tran}(t) = \begin{cases} i_1 = i_0 + \dfrac{|v_{grid}|}{L}\delta \\ i_2 = i_1 + \dfrac{|v_{grid}| - NV_{dc}}{L} T_1 \\ i_3 = i_2 + \dfrac{|v_{grid}|}{L}\left(\dfrac{T_{sw}}{2} - \delta - T_1\right) \\ i_4 = i_3 + \dfrac{-|v_{grid}|}{L}\left(T_{zp} - \dfrac{T_{sw}}{2} + \delta + T_1\right) \\ i_5 = i_4 + \dfrac{-|v_{grid}| + NV_{dc}}{L} T_2 \\ i_6 = i_5 + \dfrac{-|v_{grid}|}{L}\left(T_{zn} - \delta\right) \end{cases} \quad \text{....................}(13),$$

where L represents the sum of the transformer leakage inductance and the additional inductance, and δ is the phase difference between the primary and secondary sides [11]. Then, the relationship among the real power, the zero-voltage period, and the phase difference is given by using (14) as

$$p_g = \frac{NV_{dc}|v_{grid}|}{T_{sw}L} T_{diff}\left(2T_{diff} + T_{zp} + 2\delta - T_{sw}\right) \quad \text{..................}(14),$$

where T_{diff} represents the differential mode duration, which is equal to T_1 and T_2. When the power command p_g^* is introduced, solving equation (14) for the phase difference yields the value of phase difference δ that achieves the desired power reference, as shown in

$$\delta = \frac{1}{2}\left(T_{sw} - 2T_{diff} - T_{zp}\right) + \frac{1}{2T_{diff}} \frac{T_{sw}L}{NV_{dc} \times |v_{grid}|} p_g^* \quad \text{...........}(15).$$

The derived phase difference δ is used to control power transfer accordingly.

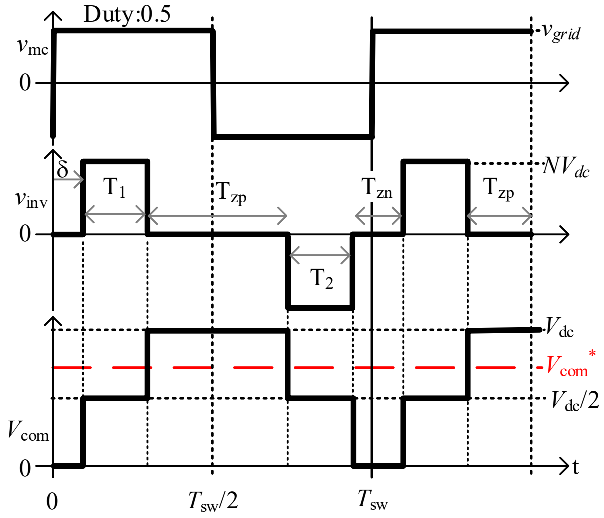

Fig. 5. Control block diagram. The zero-voltage period is calculated from the neutral-point voltage.

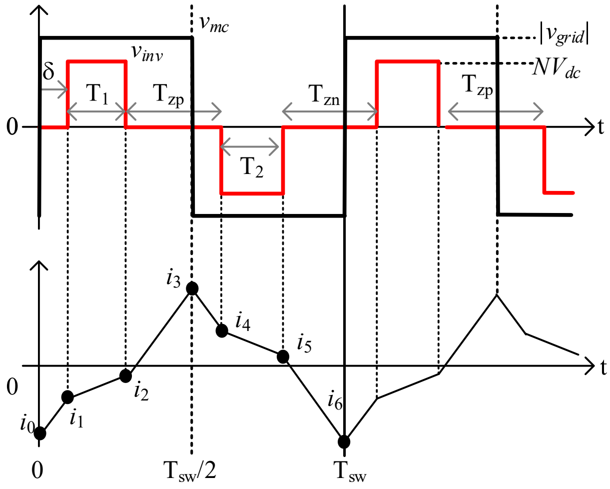

Fig. 6. Transformer voltage and current waveforms with a phase difference.

In the proposed control method, the output duration of the charging and discharging modes are intentionally made unequal to generate ripple in the center-tap voltage. As a result, the output voltages of the matrix converter and the inverter become asymmetric between the positive and negative half-cycles. Therefore, power expressions other than (14) are required depending on the operating condition. These power expressions are classified into nine cases when the phase difference is constrained to be less than 180 degrees within the control period.

Table 1 lists the decision conditions and the corresponding phase difference equations for each current mode. Each mode is identified by the parameters T_{diff}, T_{zp}, T_{zn}, and the phase difference δ. In this method, the decision process is simplified by reusing the phase difference from the previous sampling period. This approach avoids recursive calculations, which would otherwise be necessary since the original decision conditions for the phase-difference equations depend on the phase difference itself.

IV. EXPERIMENTAL RESULTS

Table 2 summarizes the experimental conditions. The inductance of the high-frequency section is less than 11 µH, which corresponds to the sum of the transformer leakage inductance and the additional inductance. The rated DC voltage is set to 250 V, assuming operation with a single-phase 100 V grid. The effectiveness of the power ripple compensation is evaluated under both power delivery and regeneration modes.

Figure 7 shows the waveforms of the primary and secondary transformer voltages, the center-tap potential, and the buffer current. The matrix converter operates with a duty ratio of 0.5, and the secondary-side inverter operates as a three-level inverter with a zero-voltage period. The center-tap potential includes both charging and discharging modes within a control period via the differential mode, with the discharging mode lasting longer than the charging mode. The current flowing out of the buffer exceeds the inflowing current, resulting in a decrease in the buffer capacitor voltage. These results confirm that the proposed asymmetric control of the charging and discharging modes functions as intended.

Figures 8(a) and 8(b) show experimental results without and with the proposed power ripple compensation, respectively. Without the proposed method, the buffer capacitor voltage v_{cbuf} remains constant, and the DC output current contains a 100 Hz ripple component. With the proposed method, the buffer current includes a ripple component, while the ripple in the DC current is reduced.

Figure 9 presents the frequency-domain analysis of the DC current. In this analysis, the 50 Hz output frequency is treated as the fundamental frequency. The amplitude of the second-harmonic component is reduced by 82% when the proposed method is applied, compared to the case without the power ripple compensation.

V. CONCLUSIONS AND FUTURE WORK

This paper has proposed a power ripple compensation method for single-phase grid applications that does not require additional switches and can be applied to DAB-type matrix converters. The proposed method controls the current between the DC source and the buffer circuit by switching the secondary-side inverter between charging and discharging modes and regulating the center-tap potential. The proposed approach achieves a high power factor while effectively compensating for single-phase power ripple. Experimental verification using a prototype converter demonstrated 500-W bidirectional power transfer under single-phase grid connections. The experimental results showed an 82% reduction in DC-side power ripple, thereby validating the effectiveness of the proposed compensation method.

Future work will focus on simplifying the phase-difference decision process and verifying the practicality of the proposed approach by increasing the transmission power and conducting experiments under higher grid-voltage conditions relevant to high-voltage systems applications.

Table 1. List of phase difference equations for each current mode.

Mode	Discriminant	Phase-difference equations
	$T_{zp}=T_{zn}$	
1	$\delta_Z<T_z$	$\delta=\frac{1}{2}\left(T_{sw}-2T_{diff}-T_{zp}+{}^{x}\!/\!_{T_{diff}}\right)$
2	$\delta_Z>T_z$	$\delta=\frac{1}{2}\left(T_{sw}-T_{diff}\right)+\frac{1}{2}\sqrt{D_1-2x}$
	$T_{zp}>T_{zn}$	
3	$\delta_Z<T_{zn}$	$\delta=\frac{1}{2}\left(T_{sw}-2T_{diff}-T_{zp}+{}^{x}\!/\!_{T_{diff}}\right)$ Same as Mode1
4	$\delta_Z+T_{diff}<\frac{T_{sw}}{2}$	$\delta=\frac{1}{2}\left(T_{sw}+T_{zn}-T_{zp}\right)-\frac{1}{2}\sqrt{D_2-4x}$
5	$\delta_Z+T_{diff}>\frac{T_{sw}}{2}$	$\delta=\frac{1}{2}\left(T_{sw}+T_{diff}+\frac{T_{zn}}{2}-\frac{T_{zp}}{2}\right)-\frac{1}{4}\sqrt{D_3-8x}$
6	$\delta_Z-T_{zn}-T_{diff}>0$	$\delta=\frac{1}{2}\left(T_{sw}-2T_{diff}\right)-\sqrt{T_{diff}^2+T_{zn}T_{diff}-x}$
	$T_{zp}<T_{zn}$	
7	$\delta_Z+T_{diff}+T_{zp}<\frac{T_{sw}}{2}$	$\delta=\frac{T_{sw}}{2}-2T_{diff}-T_{zp}-\sqrt{T_{diff}^2+T_{zn}T_{diff}-x}$
8	$\delta_Z+T_{diff}<\frac{T_{sw}}{2}$	$\delta=\frac{1}{2}\left(T_{sw}-2T_{diff}-T_{zp}\right)+\frac{x}{2T_{diff}}$
9	$\delta_Z+T_{diff}>\frac{T_{sw}}{2}$	$\delta=\frac{T_{sw}}{2}-\sqrt{T_{diff}^2+T_{zp}T_{diff}-x}$
10	$\delta_Z>T_{zn}$	$\delta=\frac{1}{2}\left(T_{sw}-T_{diff}+\frac{T_{zn}}{2}-\frac{T_{zp}}{2}\right)-\frac{1}{4}\sqrt{D_4-8x}$
Given	$\begin{cases} x=power\times \mathrm{T}_{sw}L/\left(NV_{dc}\times\lvert v_{grid}\rvert\right) \\ D_1=2T_{sw}\left(T_{diff}+T_{zp}\right)-\frac{1}{2}-T_{diff}^2-2T_{diff}T_{zp}-2T_{zp}^2 \\ D_2=T_{sw}\left(2T_{zn}+2T_{zp}+4T_{diff}\right)-\left(1+\left(T_{zp}+T_{zn}\right)^2+4T_{diff}T_{zp}\right) \\ D_3=T_{sw}\left(8T_{diff}+4T_{zn}+4T_{zp}\right)+K \\ K=-2T_{sw}^2-4T_{diff}\left(T_{diff}-T_{zn}-T_{zp}\right)-3T_{zn}^2-2T_{zn}T_{zp}-3T_{zp}^2 \end{cases}$	

Table 2. Circuit parameters

Conditions	Symbol	Value
Switching frequency	f_{sw}	50 kHz
Power	P_{ave}	500 W
Grid voltage	v_{ac}	100 $\mathrm{V_{RMS}}$
Grid frequency	f_g	50 Hz
AC filter capacitor	C_{ac}(%Y)	6.6 µF(4.1%)
AC filter inductor	L_{ac}(%Z)	45 µH (0.07%)
Buffer capacitor	$C_{buf}(\tau_c)$	510 µF (41ms)
DC-source voltage	V_{dc}	250 V
DC filter capacitor	$C_f(\tau_c)$	25 µF (8ms)
Leakage inductor	L	10 µH
Turn ratio(Pri.:Sec.)		0.6:(1:1)

REFERENCES

[1] International Energy Agency, *Global EV Outlook 2025*, IEA, Paris, 2025. [Online]. Available: https://www.iea.org/reports/global-ev-outlook-2025

[2] P. Papamanolis, F. Krismer and J. W. Kolar, "22 kW EV Battery Charger Allowing Full Power Delivery in 3-Phase as well as 1-Phase Operation," 2019 10th International Conference on Power Electronics and ECCE Asia (ICPE 2019 - ECCE Asia), Busan, Korea (South), 2019, pp. 1-8

[3] A. Ali, H. H. H. Mousa et al.: "A Comprehensive Review on Charging Topologies and Power Electronic Converter Solutions for Electric

Vehicles", Journal of Modern Power Systems and Clean Energy, vol. 12, no. 3, pp. 675-694, May 2024

[4] B. Jie, J. Baba, and A. Kumada, "Contribution to V2G System Frequency Regulation by Charging/Discharging Control of Aggregated EV Group, " in IEEE Transactions on Industry Applications, vol. 60, no. 1, pp. 1129-1140, Jan.-Feb. 2024

[5] M. Chen, K. K. Afridi and D. J. Perreault, "Stacked Switched Capacitor Energy Buffer Architecture, " in IEEE Transactions on Power Electronics, vol. 28, no. 11, pp. 5183-5195, Nov. 2013,

[6] Z. Liao and R. C. N. Pilawa-Podgurski, "Power Harmonic Elimination Technique for Using Non-linear Ceramic Capacitors under Large Voltage Swings for Single-Phase Active Power Decoupling," 2020 IEEE 21st Workshop on Control and Modeling for Power Electronics (COMPEL), Aalborg, Denmark, 2020, pp. 1-7

[7] H. Kim et al. "A Single-Stage Electrolytic Capacitor-Less EV Charger With Single- and Three-Phase Compatibility, " in IEEE Transactions on Power Electronics, vol. 37, no. 6, pp. 6780-6791, June 2022

[8] W. Kodaka, S. Ogasawara, K. Orikawa, "Power Decoupling Control of Single-Phase or Three-Phase Input High-Frequency Single-Phase Output Matrix Converters", IEEJ Transactions on Industry Applications, vol. 142, no. 1, pp.41-49, 2021(in Japanese)

[9] S. Takuma, K. Kiri, H. Watanabe and J. Itoh, "Surge Voltage Reduction Method for DAB Matrix Converter using Circulating Current in Whole Load Condition, " 2021 IEEE Energy Conversion Congress and Exposition (ECCE), Vancouver, BC, Canada, pp. 2301-2307, 2021

[10] J.Itoh, I.Sato, H.Ohguchi, K,Sato, A.Odaka, N.Eguchi: A Control Method for the Matrix Converter Based on Virtual AC/DC/AC Conversion Using Carrier Comparison Method IEEJ Vol.124-D No.5,2004(in Japanese).

[11] D. Das, N. Weise, K. Basu, R. Baranwal and N. Mohan, "A Bidirectional Soft-Switched DAB-Based Single-Stage Three-Phase AC–DC Converter for V2G Application," in IEEE Transactions on Transportation Electrification, vol. 5, no. 1, pp. 186-199, March 2019

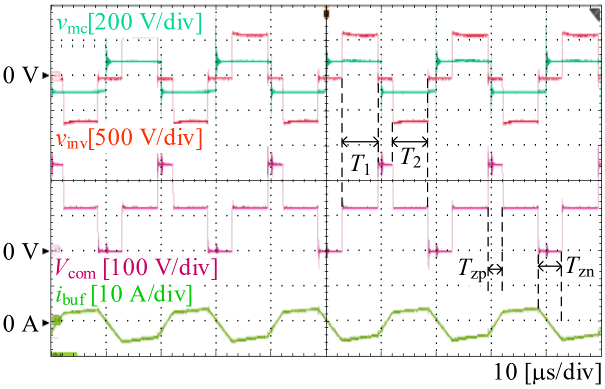

Fig. 7. High-frequency operating waveform.

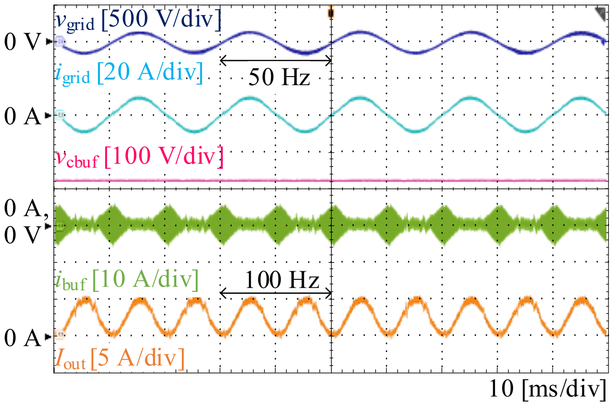

(a)Without the power decoupling method.

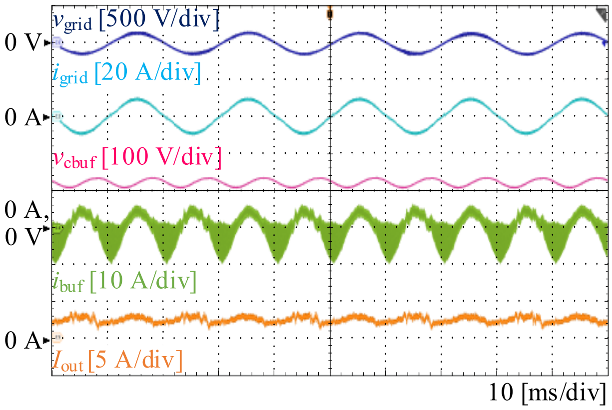

(b)With the power decoupling method.
Fig. 8. Experimental waveforms.

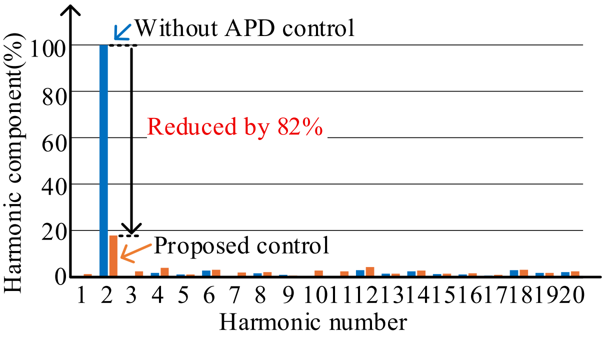

Fig. 9. Output current frequency analysis results.